npj | computational materials

Article

Published in partnership with the Shanghai Institute of Ceramics of the Chinese Academy of Sciences

https://doi.org/10.1038/s41524-025-01954-2

Probing entropic control of stacking phase preference in layered oxide cathodes for sodium-ion batteries *via* machine-learning potentials

Check for updates

Liang-Ting Wu[1,2], Zhong-Lun Li[1], Shih-Ying Yen[1], Payam Kaghazchi[2,3] & Jyh-Chiang Jiang[1] ✉

High-entropy layered oxides are promising sodium-ion battery (SIB) cathodes, yet the fundamental role of conformational entropy in stacking phase preference remains unclear. Here, we combine density functional theory (DFT), ab initio molecular dynamics (AIMD), and a fine-tuned CHGNet machine-learning interatomic potential (MLIP) to investigate representative high-entropy ($Na_{0.8}Ni_{0.2}Fe_{0.2}Co_{0.2}Mn_{0.2}Ti_{0.2}O_2$) and low-entropy ($Na_{0.8}Mn_{0.6}Co_{0.4}O_2$) layered oxides in both O3 and P2 phases. A three-stage Monte Carlo sampling strategy was developed to explore transition-metal arrangements, Na/vacancy distributions, and representative low-energy conformations. The fine-tuned CHGNet achieved near-DFT accuracy while enabling large-scale sampling at orders of magnitude lower cost. Our analyses reveal that high-entropy oxides exhibit stronger Na–TMO_2 interactions, broader O–TM bond length distributions, and smaller interlayer distance ratios compared with their low-entropy counterparts. These structural features favor O3-phase stabilization in cases where conventional ionic-potential descriptors are insufficient to clearly distinguish between O3- and P2-type layered oxides. Bond-length analyses further indicate that Jahn–Teller distortions in Mn are mitigated in high-entropy oxides, contributing to enhanced structural stability. This study establishes conformational entropy as a decisive factor, alongside Na ionic and cationic potentials, in governing stacking phase stability, and highlights the power of MLIP-accelerated modeling for exploring high-entropy materials and guiding the rational design of next-generation SIB cathodes.

After more than 30 years of development, lithium-ion batteries (LIBs) have dominated the rechargeable battery market[1–4]. At the same time, global energy demand is expected to grow explosively due to the continuous expansion of electric vehicles and consumer electronics[5,6]. In parallel, the transition to green energy requires overcoming the intermittency of renewable sources[7]. Therefore, a large-scale energy storage system with high safety, long lifespan, and high energy density is essential to meet the rising energy demand[8,9]. Although the large-scale production of LIBs is technically mature, they still face challenges such as safety concerns[10–12], limited abundance of Li precursors[13,14], high cost[15], and poor low-temperatures performance[16,17]. Sodium-ion batteries (SIBs) have attracted significant attention because Na is abundant and inexpensive[18–20]. Moreover, SIBs exhibit higher operational stability and allow faster charging compared with LIBs[21–23]. These favorable characteristics make SIBs highly suitable for large-scale battery energy storage station applications.

Layered sodium transition metal oxides (Na_xTMO_2) are promising cathode materials for SIBs, as they exhibit a wide working voltage and can be synthesized relatively easily[24,25]. The stacking phase of layered oxides significantly influences their material properties. Among them, the O3 and P2 phases are well known and widely used as cathode materials, each with distinct Na ion coordination environments. Specifically, Na ions are coordinated by six O atoms in octahedral sites in the O3 phase and in prismatic sites in the P2 phase (Fig. 1a)[26]. The O3-type oxide offers high energy capacity but suffers from irreversible phase transitions, low coulombic efficiency, and poor Na-ion diffusion[27–30]. In contrast, the P2-type

[1]Department of Chemical Engineering; Sustainable Electrochemical Energy Development (SEED) Center, National Taiwan University of Science and Technology, Taipei, Taiwan. [2]Materials Synthesis and Processing (IMD-2), Institute of Energy Materials and Devices, Forschungszentrum Jülich GmbH, Jülich, Germany. [3]MESA+ Institute, University of Twente, Enschede, The Netherlands. ✉e-mail: jcjiang@mail.ntust.edu.tw

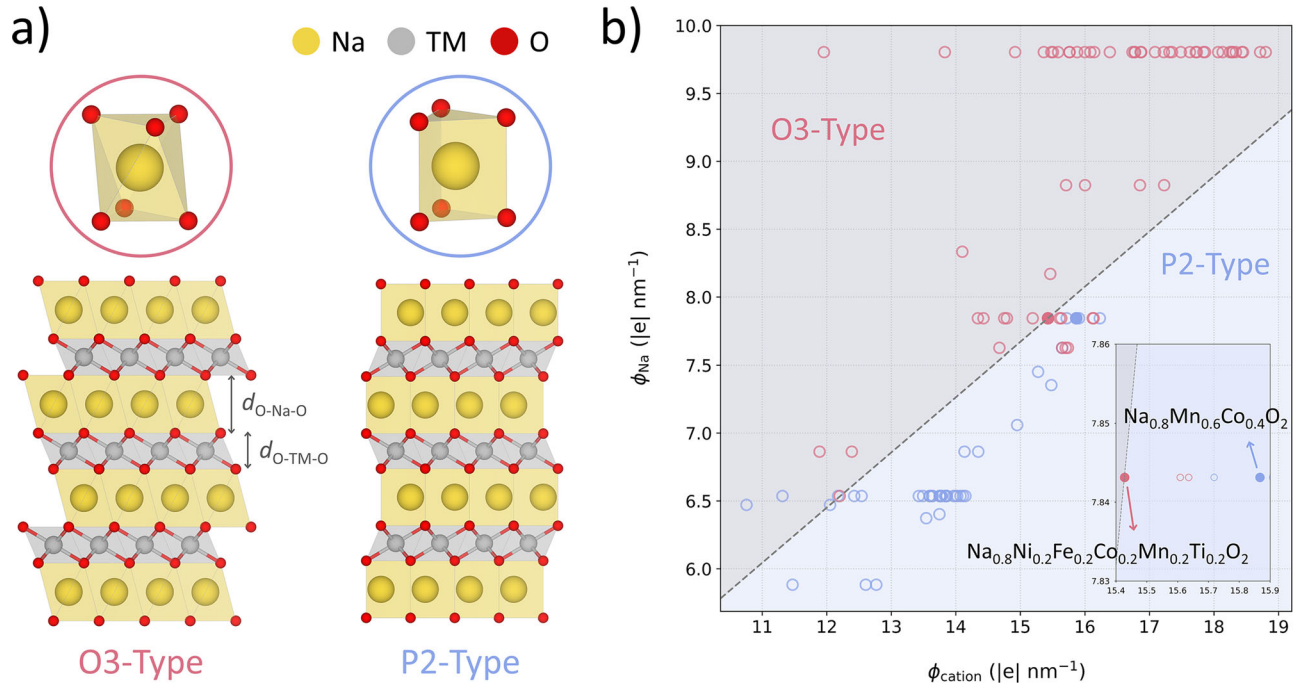


Fig. 1 | Structural geometries and phase classification of layered oxide cathodes. **a** Stacking geometries of O3- and P2-type layered oxide cathode materials in SIBs. The interlayer distance between two TMO_2 layers is denoted as d_{O-Na-O}, and the interlayer distance between two NaO_2 layers is denoted as d_{O-TM-O}. **b** Cationic potential and Na ionic potential of $Na_{0.8}Ni_{0.2}Fe_{0.2}Co_{0.2}Mn_{0.2}Ti_{0.2}O_2$ (HE) and $Na_{0.8}Mn_{0.6}Co_{0.4}O_2$ (LE), along with 102 compositions reported in Ref 65. The gray dashed line represents the classification boundary between O3 and P2 phases. Blue and pink circles represent P2- and O3-type compositions, respectively.

oxide provides faster Na ion diffusion, greater structural stability, but relatively lower energy capacity[28,31,32]. Nevertheless, high-entropy layered oxides have been demonstrated as promising cathode materials. For instance, O3-type $Na_{0.8}Ni_{0.2}Fe_{0.2}Co_{0.2}Mn_{0.2}Ti_{0.2}O_2$ exhibits a reversible O3–P3 phase transition during desodiation and retains 90% capacity after 100 cycles[33]. According to extended X-ray absorption fine structure (EXAFS) and ex situ X-ray absorption near-edge structure (XANES) spectra, Anang et al. proposed that $Ni^{2+/4+}$, $Fe^{3+/4+}$, and $Co^{3+/4+}$ redox reactions contribute to charge compensation during desodiation, while Mn^{4+} and Ti^{4+} stabilize the structure[33]. Liu et al. synthesized P2-type $Na_{0.67}Mn_{0.6}Cu_{0.08}Ni_{0.09}Fe_{0.18}Ti_{0.05}O_2$, which delivers a high capacity of 158.1 mAh g^{-1} and an initial coulombic efficiency of 98.2%[34]. Compared with P2-type $Na_{0.67}MnO_2$, the introduced Cu^{2+} and Ni^{2+} enhance oxygen-redox activity and facilitate Na^+ extraction, while Fe^{3+} and Ti^{4+} improve structural stability and suppress phase transitions in deeply desodiated states. Furthermore, the activated oxygen redox contributes additional charge capacity[34]. O3-type $Na[FeCoNiTi]_{1/6}Mn_{1/4}Zn_{1/12}O_2$ demonstrates excellent low-temperature performance (109.6 mAh g^{-1} at −20 °C, 0.1 C)[35], and O3-type $Na_{0.9}Ni_{0.2}Fe_{0.2}Co_{0.2}Mn_{0.2}Ti_{0.15}Cu_{0.05}O_2$ exhibits long-term cycling stability (79.4% capacity retention after 2000 cycles at 5 C) and outstanding rate capability (98.6 mAh g^{-1} at 10 C)[36]. The improvements in rate capability and low-temperature performance arise because the high-entropy strategy minimizes O3–P3 phase transitions during desodiation, thereby facilitating Na^+ transport. However, the fundamental understanding of interatomic interactions in high-entropy systems remains elusive, necessitating advanced atomic-level characterization approaches such as computational modeling.

Density functional theory (DFT) and ab initio molecular dynamics (AIMD) simulations[37–42], have been highly successful in modeling battery systems at the atomistic level. However, the high computational cost of DFT and AIMD limits their application to larger systems[43–45]. (Reactive) force fields can extend simulations to ~10^1 nm over ~10^1 ns[46–51], but they are less accurate than DFT. Machine-learning interatomic potentials (MLIPs), when trained on DFT data, have demonstrated remarkable accuracy and exceptional computational efficiency, making them promising methods that combine the advantages of ab initio approaches and force fields[52–57]. Schütt et al. developed the SchNet model based on continuous-filter convolutional layers, achieving rotationally invariant energy predictions and rotationally equivariant, energy-conserving force predictions for molecules[58]. Chen et al. introduced the MEGNet model, successful for both molecular and crystalline systems[59]. The same group later developed M3GNet, which explicitly incorporates three-body interactions through stacked graph convolution layers, functioning as a universal MLIP covering 89 elements[60,61]. Deng et al. advanced this field with CHGNet, pre-trained on over 1.5 million DFT data points from the Materials Project Trajectory dataset[62]. CHGNet incorporates charge information by training with magnetic moments, enabling oxidation-state-resolved predictions, particularly useful for cathode materials. Most recently, Ko et al. released the Materials Graph Library (MatGL)[63], which integrates state-of-the-art GNN-based models, significantly enhancing accessibility and accelerating data-driven, high-throughput materials discovery.

In this work, we selected two representative layered oxides, a high-entropy O3-type ($Na_{0.8}Ni_{0.2}Fe_{0.2}Co_{0.2}Mn_{0.2}Ti_{0.2}O_2$[33], HE) and a low-entropy P2-type ($Na_{0.8}Mn_{0.6}Co_{0.4}O_2$[64], LE), to investigate the entropy effects on stacking phase preference. We sampled possible conformations for four systems (O3-LE, P2-LE, O3-HE, and P2-HE) based on Coulomb energies, followed by structural optimization using DFT calculations, and performed AIMD simulations to explore the energy-minimum configurations. The resulting DFT-calculated data were then used to fine-tune the pre-trained CHGNet model. Furthermore, we developed a three-stage Monte Carlo (MC) procedure for TM and Na/vacancy sampling with the fine-tuned CHGNet. Na interaction energy and geometric analyses were subsequently performed on the final screened low-energy representative conformations. This work reveals the critical role of conformational entropy in determining stacking phase preference in layered oxide materials, providing new insights for rational cathode design and advancing the development of next-generation high-performance SIBs.

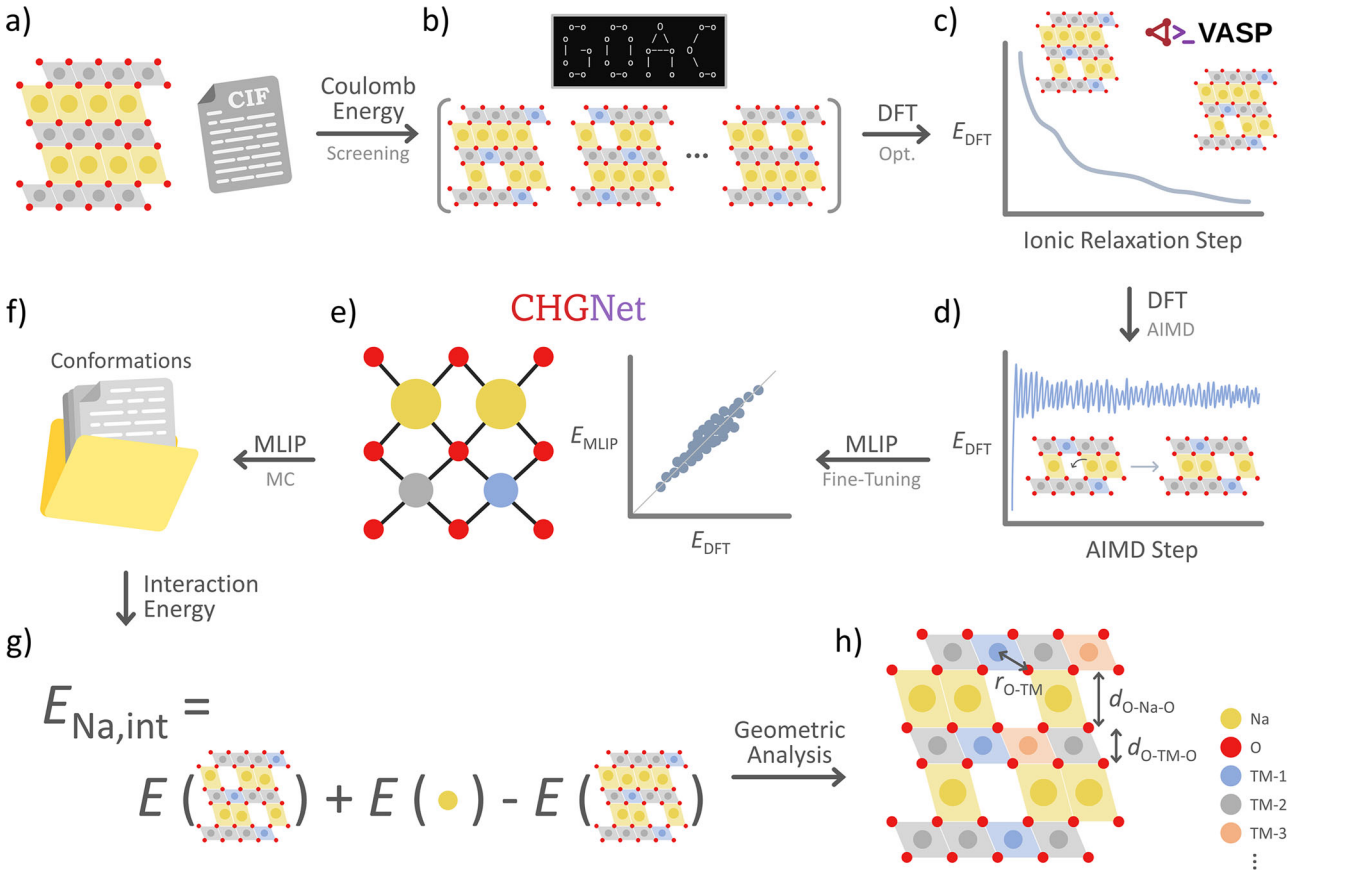


Fig. 2 | Computational workflow for analyzing entropy effects on phase preference in layered oxides. The process includes: **a** Preparation of parent structures, where O3- and P2-phase $NaCoO_2$ are adopted; **b** Conformation exploration using the GOAC code; **c** Structural optimization with DFT implemented in VASP; **d** AIMD simulation with DFT; **e** MLIP fine-tuning using datasets from AIMD simulations under the CHGNet architecture; **f** Collection of all identified low-energy conformations of O3-HE, P2-HE, O3-LE, and P2-LE layered oxides as the dataset for further analysis; **g** Subsequent energy analysis by calculating Na interaction energy; **h** Geometric analyses of O3-LE, P2-LE, O3-HE, and P2-HE layered oxide materials. The different colors of TMO_6 represent the various types of TMs contained in the layered oxides.

Results

Conformational entropy and conformation sampling of layered oxides

Investigating the role of conformational entropy in the stacking phase preference of high-entropy cathode materials requires decoupling conformational entropy from the well-known descriptors. We selected two representative layered oxide cathode materials, high-entropy $Na_{0.8}Ni_{0.2}Fe_{0.2}Co_{0.2}Mn_{0.2}Ti_{0.2}O_2$ (denoted as HE) and low-entropy $Na_{0.8}Mn_{0.6}Co_{0.4}O_2$ (denoted as LE), because they share the same Na ionic potential (ϕ_{Na}) and exhibit similar cationic potential (ϕ_{cation}), which are two major descriptors proposed by Zhao et al.[65] The ionic potential of element i (ϕ_i) is defined as the charge carried by i divided by its ionic radius (Eq. 1). Thus, a smaller ionic radius or a higher oxidation state yields a larger ionic potential, which can be viewed as a measure of electron-cloud polarizability and a descriptor of ionic character. For example, Na^+ has an ionic radius of 1.02 Å and a + 1 charge, giving an ionic potential of $9.80x$ |e| nm^{-1}, where x is the Na content in Na_xTMO_2; in this case, the Na ionic potential directly reflects the Na amount in layered oxides. The TM ionic potential (ϕ_{TM}) is the composition-weighted average of the ionic potentials of the constituent TMs (Eq. 2), and the cationic potential combines ϕ_{Na}, ϕ_{TM}, and ϕ_O as defined in Eq. 3. A higher ϕ_{TM} corresponds to TMs with higher oxidation states and smaller ionic radii. As explained by Zhao et al.[65], a larger TM ionic potential increases electrostatic repulsion between adjacent TMO_2 layers, favoring the P2 stacking phase; conversely, a larger Na ionic potential (i.e., more Na in the NaO_2 layers) screens this repulsion and favors the O3 stacking phase. Experimentally, HE and LE were confirmed to be O3- and P2-type layered oxide materials, respectively. Figure 1b presents the sodium ionic potential and cationic potential of HE and LE, along with data for 102 layered oxides from the reported dataset. Both HE and LE have a sodium ionic potential of 7.84 |e| nm^{-1} due to the same Na content (80% occupation). LE shows a slightly higher cationic potential of 15.87 |e| nm^{-1} compared with HE (15.43 |e| nm^{-1}), which can be attributed to the high ionic potential of Mn^{4+} species in LE. Nevertheless, the cationic potential difference between HE and LE is negligible compared with the wide span observed in the dataset. In contrast, the conformational entropy of HE (1.609R) and LE (0.673R) exhibits a significant gap[66]. Therefore, conformational entropy can be decoupled from both cationic potential and Na ionic potential in the comparison of HE and LE, enabling a clearer investigation of the role of conformational entropy in the stacking phase preference of layered oxides.

To better describe the interatomic interactions of layered oxide materials, it is essential to generate numerous data points with DFT-level accuracy for fine-tuning the pre-trained universal MLIP. In particular, the possible conformations of a small simulation box containing 60 TM atoms can reach approximately 4.6×10^{50} and 5.04×10^{28} for HE and LE, respectively. Although the number of conformations decreases slightly after considering symmetry, it is still impossible to evaluate all possibilities, making it challenging to identify representative conformations. Figure 2 presents the flowchart of MLIP fine-tuning. We first employed the GOAC code[67] to perform a fast conformational search for O3- and P2-type LE and HE, denoted as O3-LE, P2-LE, O3-HE, and P2-HE, considering only the Coulomb energy of each conformation. Ten conformations of each system

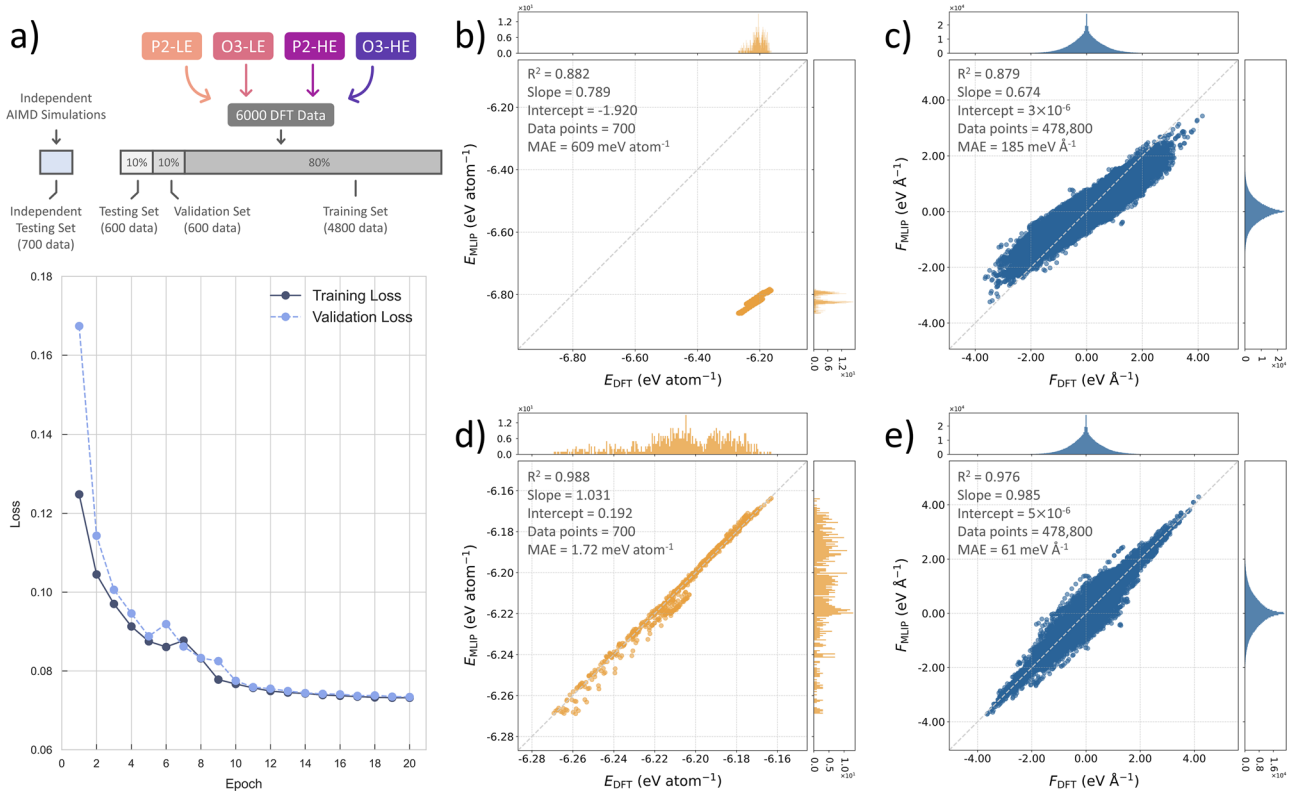


Fig. 3 | CHGNet model fine-tuning and its predictive accuracy for energies and forces. a Schematic illustration of splitting DFT data into training, validation, and testing sets, and the evolution of loss with training epochs. Predicted vs. DFT-calculated **b** energy and **c** force of the independent testing set for the pre-trained CHGNet model. Predicted vs. DFT-calculated **d** energy and **e** force of the independent testing set for the fine-tuned CHGNet model.

(O3-LE, P2-LE, O3-HE, and P2-HE) were then selected, and their geometries were further optimized using DFT. Subsequently, the three conformations with the lowest electronic energies were chosen for each layered oxide, and AIMD simulations were performed on these conformations to generate datasets for MLIP fine-tuning. This process also enabled further geometric relaxation involving barriers that might not be captured during static structural optimization, such as Na migration or TMO_6 distortion. The energy fluctuations during AIMD simulations are shown in Fig. S1. After MLIP fine-tuning, the refined model was employed to efficiently screen low-energy conformations of layered oxides, even in larger simulation cells, through TM and Na/vacancy sampling using MC simulations. The Coulomb energy and DFT-calculated electronic energy of each conformation are listed in Table S1. Subsequently, energy and geometric analyses of the selected representative conformations highlighted the critical role of conformational entropy in determining the stacking phase preference of layered oxides.

Fine-tuning of pre-trained MLIP and MLIP-based MD simulations

We collected the calculated electronic energy and geometry data from AIMD simulations to fine-tune a pre-trained universal MLIP model, CHGNet. The fine-tuning dataset was obtained from the first 500 steps of twelve independent AIMD simulations, corresponding to three distinct conformations for O3-LE, P2-LE, O3-HE, and P2-HE layered oxides. In total, 6000 DFT data points were collected and randomly split into training, validation, and testing sets with a ratio of 80:10:10, as illustrated in Fig. 3a. The loss of the CHGNet model decreased significantly with training epochs, stabilized after 10 epochs, and converged by 20 epochs. The fine-tuned CHGNet achieved losses as low as 0.0732 and 0.0734 for the training and validation sets, respectively. The performance of the pre-trained CHGNet in predicting energy and force was evaluated on the testing set, with results shown in Figs. S2a and S2b. Although the predicted energies exhibited a strong positive correlation with DFT-calculated values, the large intercept of -1.456 eV atom^{-1} in the fitted line indicated that the pre-trained CHGNet systematically underestimated the energy. For force prediction, the slope of the fitted line was only 0.715, implying an underestimation of force magnitudes. After fine-tuning, the mean absolute error (MAE) of energy was reduced from 616 meV atom^{-1} to 0.73 meV atom^{-1}, and the MAE of force decreased from 222 meV Å^{-1} to 67 meV Å^{-1}. The predicted energy and force of the testing set after fine-tuning are shown in Figs. S2c and S2d, respectively.

Although the data in the testing set were not used during model fine-tuning, they were initially split from the original 6000-point AIMD trajectory, indicating that the testing, training, and validation sets may be highly correlated and similar. To demonstrate that the fine-tuned CHGNet model generalizes well to other conformations, we selected the remaining 28 conformations screened by the GOAC code that were not used to generate AIMD data for fine-tuning; specifically, they have relatively higher electronic energies than the 12 conformations used for fine-tuning. We performed short AIMD simulations (25 steps each) for these 28 conformations, designating them as an independent testing set with 700 DFT-level data points. This independent testing set is substantially different from the training set because it was collected from different AIMD runs and from different conformations. Figure 3b and 3c show the predictive performance of the pre-trained CHGNet model on the independent testing set for energy and force, respectively. The large energy deviations and the underestimation of force are consistent with its performance on the original testing set. After fine-tuning, the MAE of energy decreased from 609 to 1.72 meV atom^{-1} (Fig. 3d), and the MAE of force was reduced from 185 to 61 meV Å^{-1} (Fig. 3e). The R^2 values for energy and force predictions reached 0.988 and 0.976 demonstrating that the fine-tuned CHGNet can predict the energy and force of HE and LE layered oxide materials with near-DFT accuracy.

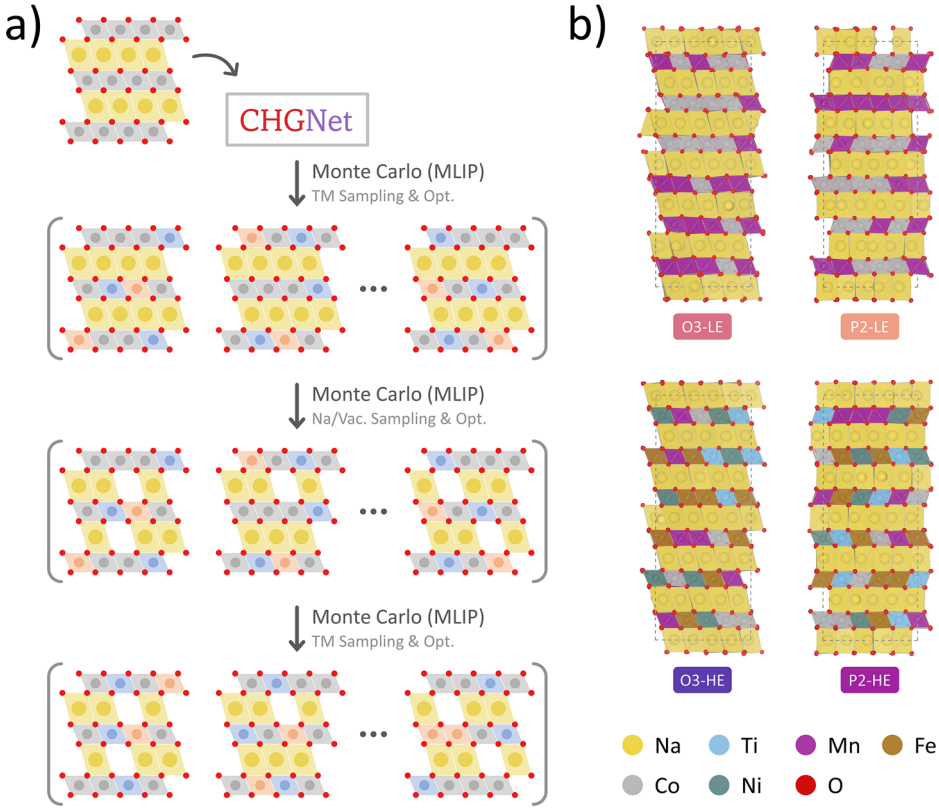


Fig. 4 | Monte Carlo (MC) simulation workflow and resulting optimized layered oxide structures. **a** Schematic illustration of the MC simulation performed using the fine-tuned CHGNet model. Stages 1, 2, and 3 correspond to TM sampling, Na/vacancy sampling, and TM re-sampling, respectively. Each MC step involves pairwise position exchanges followed by partial structural optimization. **b** Fully optimized structures of O3-LE, P2-LE, O3-HE, and P2-HE layered oxides.

Monte Carlo simulations for conformation search

Given that the fine-tuned CHGNet model has been demonstrated to accurately describe the interatomic interactions of both HE and LE layered oxides while remaining computationally efficient, we employed it to search for stable conformations of HE and LE layered oxides in large systems. We selected the $5 \times 5 \times 2$ and $5 \times 5 \times 3$ supercells for O3- and P2-type layered oxides, respectively, since they each contain 150 TM atoms, ensuring that the number of individual TM elements in the system is an integer. For example, HE layered oxides contained 30 Ni, 30 Fe, 30 Co, 30 Mn, and 30 Ti, while LE layered oxides contained 90 Mn and 60 Co. Figure 4a illustrates the flowchart of the conformation search strategy using an MLIP-based MC simulation. We began with a $NaCoO_2$ supercell containing only Co as the TM species with fully occupied Na sites, and then replaced all Co atoms with the target TM atoms in the desired proportions. Subsequently, random pairwise atom exchanges were performed to propose new conformations. A newly proposed conformation was directly accepted if its calculated energy was lower than that of the current conformation; otherwise, acceptance followed a probability that decayed exponentially with the energy difference between the two conformations. To screen representative conformations for HE and LE layered oxides, we designed a three-stage MC simulation strategy. Stage 1 involved TM sampling, in which pairwise TM atoms located at 150 TM sites were randomly exchanged under the composition $Na_{150}TM_{150}O_{300}$ until convergence or the maximum iteration was reached. The energy profile along the MC simulation steps in Stage 1 is shown in Fig. S3, and the five lowest-energy conformations were selected as inputs for Stage 2. Stage 2 focused on Na and vacancy sampling. Five independent MC simulations were performed, corresponding to the five distinct conformations obtained from Stage 1. During this stage, 150 Na atoms were reduced to 120 Na atoms with 30 vacancies to achieve an occupancy of 0.8 in both HE and LE layered oxides, with the energy changes shown in Fig. S4. Because the TM positions were sampled in Stage 1 under fully occupied Na and kept fixed during Stage 2, the introduction of vacancies was expected to significantly alter the potential energy landscape of the layered oxides. Therefore, Stage 3 involved re-sampling of the TM positions under the composition $Na_{120}TM_{150}O_{300}$. Similarly, five independent simulations were conducted based on the five conformations selected from Stage 2, and the corresponding energy profiles are summarized in Fig. S5. The energy changes shown in Figs. S3–S5 include only accepted updates; rejected conformations are not displayed. The MC simulations were terminated upon convergence, defined as an energy change below 10^{-6} eV atom^{-1}, or upon reaching a maximum of 500 iterations, which was sufficient for selecting representative conformations. To broaden the search space, we performed five independent MC simulations for stages 2 and 3 to explore additional conformations.

After the three-stage MC simulation, we selected five representative conformations for each of O3-LE, P2-LE, O3-HE, and P2-HE layered oxides. A full structural optimization was then performed for all conformations to obtain their energy-minimized configurations, as only partial structural optimizations had been carried out during the MC simulations for efficiency. The most stable structures of O3-LE, P2-LE, O3-HE, and P2-HE layered oxides are illustrated in Fig. 4b. The volume, energy, maximum force, and magnetic moment fluctuations for all conformations during the full structural optimization are shown in Figs. S6–S9. Notably, the proposed MLIP-based MC simulation framework has strong potential for exploring phase transitions during desodiation, as the possible desodiated conformations can be efficiently identified, reducing computational cost by several orders of magnitude compared with ab initio methods. Moreover, such phase transitions are closely related to the intrinsic performance of cathode materials, even though electrochemical performance was not the main focus of this work.

Furthermore, we evaluated the effectiveness of the proposed three-stage MC simulation for conformation search by using smaller test systems, HE-Small ($Na_{10}Ni_3Fe_2Co_3Mn_2Ti_2O_{24}$) and LE-Small ($Na_{10}Mn_7Co_5O_{24}$), to compare MC outcomes with DFT calculations. Owing to the reduced cell size, the compositions correspond to $Na_{0.833}Ni_{0.25}Fe_{0.167}Co_{0.25}Mn_{0.167}Ti_{0.167}O_2$ and $Na_{0.833}Mn_{0.583}Co_{0.417}O_2$, which slightly deviate from the experimental ratios and those used in the large-scale models. As an example, we selected 50 O3-HE-Small conformations from the MC simulation and computed their

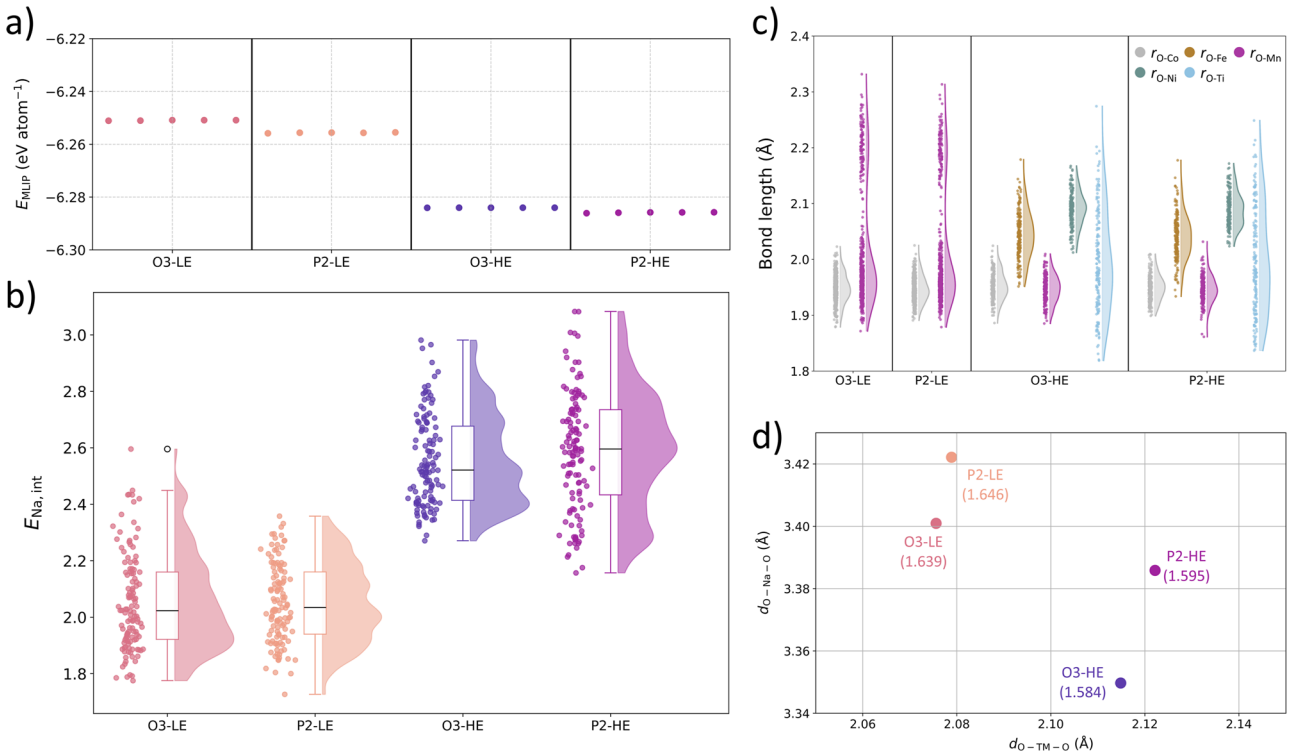


Fig. 5 | Comparative energetic and geometric analysis of the layered oxides. **a** Calculated energies of five conformations of each layered oxide. **b** Calculated Na interaction energy distributions for all selected conformations, categorized by the four layered oxides. **c** O–TM bond length distributions for the four layered oxides. **d** Average d_{O-Na-O} and d_{O-TM-O} values for the four layered oxides, with the d_{O-Na-O}/d_{O-TM-O} ratio labeled.

energies using DFT. Figure S10a shows that higher (lower) MLIP-predicted energies generally correspond to higher (lower) DFT energies. Although the MLIP–DFT correlation is not perfectly linear, the lowest-energy DFT conformation can be captured by considering a small set of top MLIP-ranked candidates. As shown in Fig. S10b, the three lowest DFT-energy conformations are ranked 4th, 2nd, and 5th by MLIP energy. Therefore, selecting more than one candidate from the MC screening is advisable to maximize the likelihood of including the true DFT minimum. The observed MLIP–DFT deviations for O3-HE-Small arise from approximations inherent to the small supercell: the Na, Ni, and Co contents are slightly higher than in the target HE composition, whereas Fe, Ti, and Mn are lower. In addition, the reduced lattice enhances inter-slab interactions, which are minimized in the larger cells used for fine-tuning.

Na interaction energy and structural analysis

Currently, we have constructed five representative conformations for each of the four layered oxide systems, and their energies are presented in Fig. 5a. Although P2-LE shows lower energy than O3-LE, P2-HE exhibits almost the same energy as O3-HE. This implies that the stacking phase preference cannot be clearly determined from the predicted energies alone. Possible reasons include the fact that the true global minimum may not have been identified, or that the stacking phase of layered oxide materials is kinetically rather than thermodynamically controlled. In practice, experimentally synthesized layered oxides rarely achieve the absolute global minimum conformation; thus, P2-type HE or the coexistence of P2 and O3 phases is often observed when the global minimum is not reached. In other words, although the calculated energy of P2-HE is slightly lower than that of O3-HE, this inconsistency with the experimentally confirmed stacking phase may not necessarily arise from the absence of true global minimum conformations. Hence, stacking phase formation during synthesis may be kinetically controlled or influenced by both thermodynamic and kinetic factors, while synthesis conditions such as temperature, pressure, and precursor composition can also affect the resulting phase. Therefore, uncovering how conformational entropy governs the interactions between Na and TMO_2 layers and shapes the structural parameters is crucial for establishing a robust mechanistic framework that reconciles theoretical predictions with experimental observations.

To investigate the role of conformational entropy in influencing the stacking phase preference of layered oxides, we defined the Na interaction energy ($E_{Na,int}$) as the energy required to remove a Na ion from the layered oxide material to its elemental state (Na metal). The Na interaction energy reflects the local interaction between a single Na ion and its surrounding environment in the material. The $E_{Na,int}$ values of 120 individual Na ions in each system were calculated using the fine-tuned CHGNet model, as shown in Fig. 5b. For the same composition (i.e., LE or HE), the P2 and O3 phases exhibited similar distributions of Na interaction energy. However, HE displayed significantly higher Na interaction energies than LE, indicating that Na ions experience stronger interactions with neighboring fragments, particularly the TMO_2 layers, in HE compared with LE layered oxides. Furthermore, we analyzed the bond lengths of distinct O–TM bonds (r_{O-TM}) within TMO_6 octahedra, as shown in Fig. 5c. For O3-LE and P2-LE, O–Mn bonds exhibited two clear distributions at approximately 1.9–2.0 Å and 2.15–2.25 Å, respectively, reflecting the Jahn–Teller distortion of Mn ions. Meanwhile, O–Co bonds were distributed within the same range as the shorter O–Mn bonds (1.9–2.0 Å). By contrast, O3-HE and P2-HE displayed highly diverse O–TM bond lengths spanning different ranges. Specifically, O–Co and O–Mn bonds both appeared at 1.9–2.0 Å, indicating that Mn ions in HE did not undergo Jahn–Teller distortion and showed only a single distribution, implying improved structural stability[68–70]. O–Fe and O–Ni bonds were longer, at 2.0–2.1 Å and 2.05–2.15 Å, respectively. The distribution of O–Ti bond lengths was much broader, ranging from 1.85 to 2.20 Å. Overall, the five TM species (Co, Fe, Mn, Ni, and Ti) in HE layered oxides exhibited different bond lengths spanning 1.85–2.20 Å, a much wider range than in LE layered oxides. This structural diversity may be the key to understanding the role of high conformational entropy in enhancing Na interaction energy and influencing the stacking phase.

Furthermore, we examined the z-coordinate distribution of O atoms, as illustrated in Fig. S11, and calculated the average z-coordinate of each O

Table 1 | Calculated descriptors, Na ionic potential, cationic potential, and conformational entropy, of HE and LE layered oxides

	HE	LE
Φ_{Na} (|e| nm^{-1})	7.84	7.84
Φ_{cation} (|e| nm^{-1})	15.43	15.87
S_{conf}	1.609 R	0.673 R
$E_{Na,int}$	Higher	Lower
r_{O-TM}	Diverse	Uniform
d_{O-Na-O}	Shorter	Longer
d_{O-TM-O}	Longer	Shorter
R	<1.62	>1.62
Stacking Phase (exp.)	O3 (Ref 33.)	P2 (Ref 64.)

Comparison of Na interaction energy, O–TM bond lengths, interlayer distances (d_{O-Na-O} and d_{O-TM-O}), interlayer distance ratios, and experimentally observed stacking phases of HE and LE layered oxides.

layer, yielding a total of twelve O layers in the layered oxide models. From these values, the average interlayer distances between TMO_2 layers (d_{O-Na-O}) and NaO_2 layers (d_{O-TM-O}), as defined in Fig. 1a, were determined and are summarized in Table S2. Among the systems, P2-LE exhibited the largest interlayer distance between two TMO_2 layers (d_{O-Na-O}) at 3.422 Å, followed by O3-LE (3.401 Å), P2-HE (3.386 Å), and O3-HE (3.350 Å) (Fig. 5d). Thus, for the same composition, the P2 phase shows a larger d_{O-Na-O} than the O3 phase. Meanwhile, HE layered oxides exhibited shorter d_{O-Na-O} values than LE layered oxides, implying stronger interactions between Na and the adjacent TMO_2 layers in HE compared with LE. In addition, P2-HE displayed the largest interlayer distance between two NaO_2 layers (d_{O-TM-O}) at 2.122 Å, followed by O3-HE (2.115 Å), P2-LE (2.079 Å), and O3-LE (2.076 Å). This indicates that the P2 phase has longer d_{O-TM-O} than the O3 phase for the same composition. Interestingly, HE layered oxides also exhibited longer d_{O-TM-O} values than LE layered oxides, suggesting weaker O–TM bonds in HE compared with LE. Finally, we calculated the ratio of d_{O-Na-O} to d_{O-TM-O} (R) for O3-LE, P2-LE, O3-HE, and P2-HE. This ratio is commonly used to identify the stacking phase of layered oxides, where $R > 1.62$ typically corresponds to P2-type and $R < 1.62$ corresponds to O3-type[65]. The calculated R values were 1.595 for P2-HE, 1.584 for O3-HE, 1.639 for O3-LE, and 1.646 for P2-LE.

In addition, we further examined four representative small systems, O3-HE-Small, P2-HE-Small, O3-LE-Small, and P2-LE-Small, as validation systems to confirm that our findings also hold within the DFT framework. As shown in Fig. S12a, we optimized the MC-screened layered oxides and evaluated their Na interaction energies (Fig. S12b) using DFT. The results show that Na–TMO_2 interactions are enhanced in the HE-Small system, consistent with the large-cell trends obtained using the fine-tuned CHGNet. The DFT-calculated Na interaction energies in the small cells are generally higher than the MLIP-predicted values in the large cells because removing one Na atom from the small system corresponds to a large concentration change (10% Na) compared with only 0.833% in the large system. Moreover, the diverse O–TM bond-length distributions observed in MLIP-relaxed geometries are successfully reproduced in the DFT-relaxed structures (Fig. S12c). The O3-HE-Small and P2-LE-Small systems exhibit the lowest and highest d_{O-Na-O}/d_{O-TM-O} ratios, respectively (Fig. S12d). Overall, these results demonstrate that our MLIP-based conclusions are valid at the DFT level, although small-cell results are inherently less representative than large-cell results due to the different lattice sizes adopted for the P2 and O3 phases and the approximate Na and TM concentrations.

Discussion

According to our calculations, O3-type layered oxides have a lower R value than P2-type layered oxides, which agrees with the conventional classification rule. The HE layered oxide exhibits a lower R value than the LE layered oxide, implying that the interaction characteristics of HE are closer to those of typical O3-type layered oxides, while the interaction characteristics of LE are similar to those of typical P2-type layered oxides. Surprisingly, the R value of P2-HE is even lower than that of O3-LE, suggesting that the interlayer distance and interaction characteristics of P2-HE resemble those of typical O3-type layered oxides commonly observed in other compositions, despite P2-HE being structurally classified as a P2 stacking phase. This also suggests that the R value is more sensitive to the materials themselves than to the stacking phase, indicating that the interlayer ratio and stacking phase are likely governed by deeper physicochemical principles. Based on the analyses of Na interaction energy, O–TM bond length distribution, and interlayer distances, we observed that HE layered oxides exhibit stronger Na interaction energy, more diverse O–TM bond lengths, longer d_{O-TM-O}, and shorter d_{O-Na-O} compared with LE layered oxides. These trends are consistent for both O3-HE and P2-HE, indicating that they are intrinsic features rather than stacking-phase-dependent effects. Based on these observations, we propose the following mechanism for entropic control of stacking phase preference in layered oxides. The introduction of multiple TM elements during material synthesis generates diverse O–TM interactions, as reflected in the highly varied O–TM bond lengths. This has been experimentally confirmed by Fourier-transformed extended X-ray absorption fine structure (FT-EXAFS) spectra of the high-entropy O3–type $NaFe_{0.2}Co_{0.2}Ni_{0.2}Ti_{0.2}Sn_{0.1}Li_{0.1}O_2$ layered oxide[71]. In a TMO_2 layer, each O atom bonds with three TM atoms, and differences among these bond lengths induce slight geometric distortions and displacements of TM and O atoms compared with ideal layered oxide structures. Since TM and O atoms carry positive and negative charges, respectively, such atomic displacements generate local dipole moments and non-uniform electric fields, thereby strengthening the interaction between Na ions and the TMO_2 layers. The local electrons have been shown to undergo alteration and redistribution due to atomic delocalization, thereby inducing polarized electric fields[72]. This enhanced Na–TMO_2 interaction is confirmed by the higher calculated Na interaction energies and shorter d_{O-Na-O} distances in HE compared with LE layered oxides. The elongation of d_{O-TM-O} can be attributed to the reduction of d_{O-Na-O}, resulting from the redistribution of electron density from O–TM bonds to Na–O ionic bonds. Consequently, the key to lowering the d_{O-Na-O}/d_{O-TM-O} ratio (R) lies in inducing atomic displacements and geometric distortions in the TMO_2 layers, which can be achieved by increasing the diversity of O–TM bonds. Thus, conformational entropy serves as a useful metric for evaluating the non-uniformity and diversity of O–TM interactions in high-entropy layered oxides. Importantly, the high conformational entropy of HE materials favors the O3 phase, even though their Na ionic potential and cationic potential metrics are similar to those of LE layered oxides. Table 1 provides an integrated comparison of the compositional descriptors, calculated energetic and geometric parameters, and experimentally observed stacking phases of HE and LE layered oxides.

Remarkably, the proposed relationship between O–TM interactions, Na interaction energies, and the macroscopic stacking phase preference provides a rational and universal framework for interpreting other classification descriptors, such as Na ionic potential and cationic potential. Specifically, in addition to conformational entropy, high Na ionic potential and low cationic potential usually favor the O3-phase. A lower cationic potential indicates a layered oxide containing a softer acid (TM) with a lower charge and a larger ionic radius. A softer TM results in a weaker O–TM interaction, as O is considered a hard base and interacts more strongly with a hard acid (TM with high ionic potential) based on the hard and soft acids and bases (HSAB) theory[73–75]. Similarly, a higher Na ionic potential suggests a higher Na concentration in the layered oxide, leading to a reduction in the oxidation state of TM to maintain charge balance, which causes the TM to be softer compared to layered oxides with lower Na concentration. Therefore, both low cationic potential and high Na ionic potential suggest a weaker O–TM interaction, with the O–Na interaction enhanced by electron redistribution, ultimately reducing d_{O-Na-O}, elongating d_{O-TM-O}, and lowering the R value, all of which favor the O3-phase. This proposed mechanism not only explains the relationship between all observed

descriptors and the stacking phase preference, revealing the underlying physicochemical principles, but also provides a chemical bonding perspective.

In conclusion, we developed a MC simulation strategy based on the fine-tuned CHGNet MLIP model to sample TMs, Na ions, and vacancies in Na_xTMO_2 layered oxide materials, and to investigate the role of conformational entropy in influencing stacking phase preference through energetic and geometric analysis. Specifically, we used the GOAC code to rapidly generate a series of possible conformations for the high-entropy layered oxide $Na_{0.8}Ni_{0.2}Fe_{0.2}Co_{0.2}Mn_{0.2}Ti_{0.2}O_2$ (HE) and the low-entropy oxide $Na_{0.8}Mn_{0.6}Co_{0.4}O_2$ (LE), derived from O3- and P2-type $NaCoO_2$. The selected conformations were subjected to structural optimization and AIMD simulations to generate 6000 DFT-calculated data points, which were then used for CHGNet fine-tuning. The fine-tuned CHGNet model exhibited extremely low mean absolute errors of 1.72 meV $atom^{-1}$ for energy and 61 meV $Å^{-1}$ for force. Using this fine-tuned model, we performed a three-stage MC simulation consisting of TM sampling, Na/vacancy sampling, and TM re-sampling, ultimately screening five representative low-energy conformations for each layered oxide (O3-LE, P2-LE, O3-HE, and P2-HE). HE exhibited significantly higher calculated Na interaction energy than LE, indicating stronger Na–TMO_2 interactions in HE layered oxides. Moreover, HE showed highly diverse O–TM bond lengths, which may induce atomic displacements and generate local dipoles and non-uniform electric fields, thereby enhancing Na–TMO_2 interactions. In contrast, LE exhibited Jahn–Teller distortion of Mn ions, which was mitigated in HE, implying higher structural stability for HE. Finally, HE displayed shorter d_{O-Na-O} and longer d_{O-TM-O} interlayer distances compared to LE, corresponding to strengthened Na–TMO_2 interactions and weakened O–TM interactions. This resulted in a lower interlayer ratio ($R < 1.62$) for HE than for LE. In conclusion, the high conformational entropy of HE reflects the introduction of more diverse O–TM interactions, ultimately leading to an O3-phase preference in HE when other descriptors are comparable to those of LE. This work demonstrated that the fine-tuned MLIP model can efficiently explore the low-energy conformations of high-entropy materials. The Na/vacancy sampling functionality is also highly promising for investigating the phase transition behavior of layered oxides during the desodiation process (charging), even though this issue was not discussed here. Such studies are prohibitively expensive with ab initio methods and often inaccurate with classical approaches, but become computationally affordable and reliable when employing fine-tuned MLIPs. Furthermore, we bridged atomistic interactions with the macroscopic stacking phases of layered oxides, revealing the decisive role of conformational entropy in stacking phase preference. This insight not only deepens our fundamental understanding but also provides a robust pathway toward the rational design of next-generation high-performance SIB cathodes.

Methods

Descriptors for stacking phase classification

The ionic potential descriptors were calculated based on the definitions and formulas reported by Zhao et al.[65]. The Na ionic potential (ϕ_{Na}) and O ionic potential (ϕ_O) were obtained using Eq. (1) with i = Na and O, respectively. The average ionic potential of the TMs (ϕ_{TM}) was calculated using Eq. (2), where j includes all possible TMs (e.g., Ni, Co, Mn, etc.) in the compositions. Furthermore, the cationic potential (ϕ_{cation}) was calculated using Eq. (3), defined as the product of the Na ionic potential and the average TM ionic potential, divided by the O ionic potential. In addition, the conformational entropy of the TMs (S_{conf}) was calculated using Eq. (4)[76,77], which corresponds to the ideal mixing entropy. The excess entropy of mixing in real systems was set to zero to simplify the calculation and allow evaluation without experimental data.

$$\phi_i = n_i \frac{q_i}{r_i} \tag{1}$$

$$\phi_{TM} = \sum_j n_j \frac{q_j}{r_j} \tag{2}$$

$$\phi_{cation} = \frac{\phi_{Na}\phi_{TM}}{\phi_O} \tag{3}$$

$$S_{conf} = -R\sum_j n_j \ln(n_j) \tag{4}$$

where n, q, and r represent the concentration, formal charge (oxidation state), and ionic radius of each element, respectively.

Global optimization of atomistic configurations by the Coulomb (GOAC) code

The initial configurations of Na_xTMO_2 were generated using the GOAC code[67]. The O3-type Na_xTMO_2 was derived from the parent composition O3-type $NaCoO_2$ (mp-18921 from the Materials Project)[78–80] and constructed as a 5×4×1 supercell with lattice constants a = 14.407 Å, b = 11.525 Å, and c = 15.440 Å. The P2-type Na_xTMO_2 was derived from the parent composition P2-type $NaCoO_2$ (mp-867515 from the Materials Project)[79–81] and constructed as a 5×3×2 supercell with lattice constants a = 14.386 Å, b = 8.632 Å, and c = 20.780 Å. Each configuration contained 120 O atoms, 48 Na atoms, and 60 TM atoms, equivalent to $(Na_{0.8}TMO_2)_{60}$. The smeared-charge Coulomb interaction model was employed to calculate the Coulomb energy of $Na_{0.8}TMO_2$. The oxidation states and ionic radii of the constituent elements are listed in Table S3. A random-hybrid algorithm was then used to search for possible configurations with low Coulomb energies. Fifty independent runs were performed, and ten configurations with the lowest Coulomb energies were selected for further investigation.

Density functional theory (DFT) calculations

Spin-polarized DFT calculations were performed using the projector augmented wave (PAW)[82,83] method as implemented in the Vienna Ab initio Simulation Package (VASP)[84–86]. The Perdew–Burke–Ernzerhof (PBE) generalized gradient approximation (GGA) functional was used to describe exchange–correlation interactions[87], and Grimme's DFT-D3 approach was applied to account for van der Waals corrections[88]. The electronic energy and force convergence criteria for self-consistent iterations and structural optimization were set to 10^{-4} eV and 0.015 eV $Å^{-1}$, respectively. A plane-wave cutoff energy of 520 eV was applied in all calculations. The Brillouin zone was sampled using a 2 × 3 × 2 Monkhorst–Pack grid for O3-type and a 2 × 3 × 1 grid for P2-type structures[89,90]. For the DFT + U method[91], Hubbard U values of 6.2, 5.3, 3.32, 3.9, and 5.10 eV were applied to the 3 d orbitals of Ni, Fe, Co, Mn, and Ti, respectively, following the Materials Project database[92]. The pseudopotentials Na_pv, Ni_pv, Fe_pv, Mn_pv, and Ti_pv were selected for Na, Ni, Fe, Mn, and Ti, respectively, instead of standard pseudopotentials, to ensure consistency with the Materials Project database[92].

Ab initio molecular dynamics (AIMD) simulations

The AIMD simulations were performed using VASP under the NVT ensemble with a time step of 2 fs. A Nosé–Hoover thermostat was applied to maintain a constant temperature of 600 K[93,94]. The Brillouin zone was sampled at the Γ point for all simulations. Twelve independent AIMD simulations were carried out for the selected conformations: O3-HE-1, O3-HE-2, and O3-HE-8 for O3-HE layered oxides; P2-HE-6, P2-HE-7, and P2-HE-8 for P2-HE layered oxides; O3-LE-2, O3-LE-8, and O3-LE-10 for O3-LE layered oxides; and P2-LE-5, P2-LE-6, and P2-LE-7 for P2-LE layered oxides.

Crystal Hamiltonian graph neural network (CHGNet)

The MLIP used in this work was based on the pre-trained universal model CHGNet[62] and fine-tuned with data generated from first-principles calcu-

lations (DFT and AIMD). A total of 6000 DFT data points were used for fine-tuning, with 80% (4800) assigned to the training set, 10% (600) to the validation set, and 10% (600) to the testing set. The MLIP converged within 20 epochs. The initial learning rate was set to 0.01, and the CosineAnnealingLR scheduler was applied, with a minimum learning rate of 1×10^{-4}.

Monte Carlo (MC) methods

The fine-tuned CHGNet model-based MC simulation consisted of two screening processes. The primary screening process began with target atom replacement; for example, the Co atoms in $NaCoO_2$ were replaced by various TM atoms in corresponding amounts to form Na_xTMO_2, followed by structural optimization for n iterations. Typically, n was set to a small value (e.g., 15 or 20) for computational efficiency, or the optimization was terminated once the calculated force dropped below 0.05 eV $Å^{-1}$. The corresponding energy was denoted as E_0. Next, pairwise atom exchanges were performed between two randomly selected exchangeable atoms, and the resulting structure was further optimized for n iterations. The energy of the newly proposed conformation was denoted as E_{new}. The acceptance probability was determined by comparing E_{new} with E_0 according to the Metropolis acceptance criterion[95], expressed as:

$$P(\text{accept}) = \min[1, e^{(E_0 - E_{new})/k_B T}] \quad (5)$$

where the acceptance is 1 when the E_{new} lower than E_0, and the new proposed conformation would replace the previous conformation, and E_{new} replace the E_0. In contrast, the acceptance exponentially decays along the energy difference between two conformation when the E_{new} higher than E_0. The same conformation that had previously been considered in the MC simulation was skipped to reduce computational cost. The simulation temperature was set to 400 K to allow the higher energy conformation to be accepted, preventing the solution was trapped in local minimum. The first screening process would terminated when the calculated energy change lower than 10^{-6} eV $atom^{-1}$ or reached the maximum iteration of 500. After termination of first screening process, 20 conformations with lowest energy would be selected as the input for the second screening process.

The second screening process involved the structural optimization of the 20 conformations selected from the first screening process. The maximum number of optimization iterations was extended to 100, or convergence was reached when the calculated force dropped below 0.01 eV $Å^{-1}$, which is a stricter criterion than that used in the first screening process. Finally, the five lowest-energy conformations were reported as the results of the MC simulation.

The three-stage MC simulation strategy was employed to search for representative conformations of Na_xTMO_2 layered oxides. Stage 1 was responsible for TM sampling within 150 sites, while Stage 2 involved Na and vacancy sampling within 150 sites, with only 120 sites occupied by Na. Stage 3 corresponded to TM re-sampling in the presence of vacancies. In addition, five representative conformations of each layered oxide underwent full structural optimization following the three-stage MC simulations.

Na interaction energy

The Na interaction energy of individual Na ions in layered oxides was calculated using the fine-tuned CHGNet model, as follows:

$$E_{\text{Na,int}} = E\left(Na_{119}TM_{150}O_{300}\right) + E(\text{Na}) - E\left(Na_{120}TM_{150}O_{300}\right) \quad (6)$$

where $E(Na_{119}TM_{150}O_{300})$ represents the energy of the $Na_{119}TM_{150}O_{300}$ model, corresponding to the layered oxide with one Na atom removed; $E(Na_{120}TM_{150}O_{300})$ represents the energy of the fully stoichiometric $Na_{120}TM_{150}O_{300}$ model; and E(Na) represents the energy of Na in its elemental state (Na metal), used as the reference. $E(Na_{120}TM_{150}O_{300})$ and E(Na) were calculated for fully optimized configurations, while $E(Na_{119}TM_{150}O_{300})$ was calculated for unrelaxed structures to prevent the Na interaction energy from being coupled with the energy released during geometry relaxation.

Data availability

The datasets generated and analyzed during the current study are available in https://github.com/KrisZhongLunLi/CHGNet-based-MC-sampling-toolkit.

Received: 29 September 2025; Accepted: 30 December 2025;
Published online: 14 January 2026

References

1. Goodenough, J. B. & Park, K.-S. The Li-ion rechargeable battery: a perspective. *J. Am. Chem. Soc.* **135**, 1167–1176 (2013).
2. Cheng, X.-B., Zhang, R., Zhao, C.-Z. & Zhang, Q. Toward safe lithium metal anode in rechargeable batteries: a review. *Chem. Rev.* **117**, 10403–10473 (2017).
3. Goodenough, J. B. & Kim, Y. Challenges for rechargeable Li batteries. *Chem. Mater.* **22**, 587–603 (2010).
4. Ren, X. et al. Enabling high-voltage lithium-metal batteries under practical conditions. *Joule* **3**, 1662–1676 (2019).
5. Masias, A., Marcicki, J. & Paxton, W. A. Opportunities and challenges of lithium ion batteries in automotive applications. *ACS Energy Lett.* **6**, 621–630 (2021).
6. Manthiram, A. An outlook on lithium ion battery technology. *ACS Cent. Sci.* **3**, 1063–1069 (2017).
7. Tong, D. et al. Geophysical constraints on the reliability of solar and wind power worldwide. *Nat. Commun.* **12**, 6146 (2021).
8. Killer, M., Farrokhseresht, M. & Paterakis, N. G. Implementation of large-scale Li-ion battery energy storage systems within the EMEA region. *Appl. Energy* **260**, 114166 (2020).
9. Zhu, Z. et al. Rechargeable batteries for grid scale energy storage. *Chem. Rev.* **122**, 16610–16751 (2022).
10. Feng, X. et al. Thermal runaway mechanism of lithium ion battery for electric vehicles: A review. *Energy Storage Mater.* **10**, 246–267 (2018).
11. Liu, B. et al. Safety issues caused by internal short circuits in lithium-ion batteries. *J. Mater. Chem. A* **6**, 21475–21484 (2018).
12. Liu, X. et al. Thermal runaway of lithium-ion batteries without internal short circuit. *Joule* **2**, 2047–2064 (2018).
13. Xu, H., Chen, H. & Gao, C. Advanced graphene materials for sodium/potassium/aluminum-ion batteries. *ACS Mater. Lett.* **3**, 1221–1237 (2021).
14. Balaram, V., Santosh, M., Satyanarayanan, M., Srinivas, N. & Gupta, H. Lithium: A review of applications, occurrence, exploration, extraction, recycling, analysis, and environmental impact. *Geosci. Front.* **15**, 101868 (2024).
15. Yao, A., Benson, S. M. & Chueh, W. C. Critically assessing sodium-ion technology roadmaps and scenarios for techno-economic competitiveness against lithium-ion batteries. *Nat. Energy* **10**, 404–416 (2025).
16. Wang, C.-Y. et al. Lithium-ion battery structure that self-heats at low temperatures. *Nature* **529**, 515–518 (2016).
17. Ji, Y., Zhang, Y. & Wang, C.-Y. Li-ion cell operation at low temperatures. *J. Electrochem. Soc.* **160**, A636 (2013).
18. Qahtan, T. F., Alade, I. O., AlArjani, A. & Rahaman, M. S. Advancements in sodium-ion batteries: An in-depth scientometric review. *J. Energy Storage* **131**, 117490 (2025).
19. Priyadarshi, N. in *Water Encyclopedia* 551–553.
20. Abraham, K. M. How comparable are sodium-ion batteries to lithium-ion counterparts? *ACS Energy Lett.* **5**, 3544–3547 (2020).
21. Yabuuchi, N., Kubota, K., Dahbi, M. & Komaba, S. Research development on sodium-ion batteries. *Chem. Rev.* **114**, 11636–11682 (2014).
22. Li, M. et al. Low-temperature performance of Na-ion batteries. *Carbon Energy* **6**, e546 (2024).
23. Wang, K. et al. Recent advances in Mn-rich layered materials for sodium-ion batteries. *Adv. Funct. Mater.* **33**, 2212607 (2023).

24. Kim, H.-J. et al. Synergetic impact of dual substitution on anionic–Cationic activity of P2-type sodium manganese oxide. *Energy Storage Mater.* **66**, 103224 (2024).
25. Voronina, N. et al. Synergetic lattice and surface engineering: stable high-voltage cycle performance in P3-type layered manganese oxide. *Adv. Energy Mater.* **n/a**, 2501823.
26. Delmas, C., Fouassier, C. & Hagenmuller, P. Structural classification and properties of the layered oxides. *Phys. B+C.* **99**, 81–85 (1980).
27. Voronina, N. et al. A new approach to stable cationic and anionic redox activity in O3-layered cathode for sodium-ion batteries. *Adv. Energy Mater.* **11**, 2100901 (2021).
28. Voronina, N. et al. Electronic structure engineering of honeycomb layered cathode material for sodium-ion batteries. *Adv. Energy Mater.* **11**, 2003399 (2021).
29. Ma, X. et al. Structural and electrochemical progress of O3-type layered oxide cathodes for Na-ion batteries. *Nanoscale* **15**, 14737–14753 (2023).
30. Oh, S.-M. et al. High capacity O3-Type Na[Li0.05(Ni0.25Fe0.25Mn0.5)0.95]O2 cathode for sodium ion batteries. *Chem. Mater.* **26**, 6165–6171 (2014).
31. Cho, M.-J. et al. Theoretical and Experimental Optimization of P2-Type Sodium-Ion Battery Cathodes via Li, Mg, and Ni Co-Doping: A Path to Enhanced Capacity and Stability. *Adv. Energy Mater.* **15**, 2405112 (2025).
32. Yang, L. et al. Structural Aspects of P2-Type Na0.67Mn0.6Ni0.2Li0.2O2 (MNL) Stabilization by Lithium Defects as a Cathode Material for Sodium-Ion Batteries. *Adv. Funct. Mater.* **31**, 2102939 (2021).
33. Anang, D. A. et al. O3-type layer-structured Na0.8[Ni1/5Fe1/5Co1/5Mn1/5Ti1/5]O2 as long life and high power cathode material for sodium-ion batteries. *Ceram. Int.* **45**, 23164–23171 (2019).
34. Liu, Z. et al. Achieving a Deeply Desodiated Stabilized Cathode Material by the High Entropy Strategy for Sodium-ion Batteries. *Angew. Chem. Int. Ed.* **63**, e202405620 (2024).
35. Zeng, Z. et al. High-entropy O3-type cathode enabling low-temperature performance for sodium-ion batteries. *Nano Energy* **128**, 109813 (2024).
36. Wang, X.-Z. et al. Fast Na+ Kinetics and Suppressed Voltage Hysteresis Enabled by a High-Entropy Strategy for Sodium Oxide Cathodes. *Adv. Mater.* **36**, 2312300 (2024).
37. Urban, A., Seo, D.-H. & Ceder, G. Computational understanding of Li-ion batteries. *npj Comput Mater.* **2**, 16002 (2016).
38. Wu, L.-T., Hwang, B. J. & Jiang, J.-C. Combined machine learning and computational protocols to predict electrolyte behavior and SEI formation in Li-metal batteries. *Chem. Eng. J.* **515**, 163801 (2025).
39. Ito, D., Jang, S.-H., Ando, H., Momma, T. & Tateyama, Y. Dissimilar Diffusion Mechanisms of Li+, Na+, and K+ Ions in Anhydrous Fe-Based Prussian Blue Cathode. *J. Am. Chem. Soc.* **147**, 25441–25453 (2025).
40. Wu, L.-T., Zhan, Y.-T., Chiu, Y.-C., Hwang, B. J. & Jiang, J.-C. Multifunctional Zwitterionic Self-Healing Polymer Electrolytes for Anode-Free Lithium-Metal Batteries: a Computational Perspective. *Small* **21**, 2503382 (2025).
41. Sasaki, R., Gao, B., Hitosugi, T. & Tateyama, Y. Nonequilibrium molecular dynamics for accelerated computation of ion–ion correlated conductivity beyond Nernst–Einstein limitation. *npj Comput. Mater.* **9**, 48 (2023).
42. Ko, S. et al. Electrode potential influences the reversibility of lithium-metal anodes. *Nat. Energy* **7**, 1217–1224 (2022).
43. Takenaka, N., Bouibes, A., Yamada, Y., Nagaoka, M. & Yamada, A. Frontiers in Theoretical Analysis of Solid Electrolyte Interphase Formation Mechanism. *Adv. Mater.* **33**, 2100574 (2021).
44. Spotte-Smith, E. W. C. et al. Chemical Reaction Networks Explain Gas Evolution Mechanisms in Mg-Ion Batteries. *J. Am. Chem. Soc.* **145**, 12181–12192 (2023).
45. Wen, M. et al. Chemical reaction networks and opportunities for machine learning. *Nat. Comput. Sci.* **3**, 12–24 (2023).
46. Huang, H. et al. Delocalized electrolyte design enables 600 Wh kg−1 lithium metal pouch cells. *Nature* **644**, 660–667 (2025).
47. Kim, M. S. et al. Suspension electrolyte with modified Li+ solvation environment for lithium metal batteries. *Nat. Mater.* **21**, 445–454 (2022).
48. Hou, T. et al. The influence of FEC on the solvation structure and reduction reaction of LiPF6/EC electrolytes and its implication for solid electrolyte interphase formation. *Nano Energy* **64**, 103881 (2019).
49. Islam, M. M. & van Duin, A. C. T. Reductive Decomposition Reactions of Ethylene Carbonate by Explicit Electron Transfer from Lithium: An eReaxFF Molecular Dynamics Study. *J. Phys. Chem. C.* **120**, 27128–27134 (2016).
50. Fong, K. D., Self, J., McCloskey, B. D. & Persson, K. A. Onsager transport coefficients and transference numbers in polyelectrolyte solutions and polymerized ionic liquids. *Macromolecules* **53**, 9503–9512 (2020).
51. Yu, Z. et al. Rational solvent molecule tuning for high-performance lithium metal battery electrolytes. *Nat. Energy* **7**, 94–106 (2022).
52. Zhang, Y.-W. et al. Roadmap for the development of machine learning-based interatomic potentials. *Model. Simul. Mater. Sci. Eng.* **33**, 023301 (2025).
53. Ko, T. W. & Ong, S. P. Recent advances and outstanding challenges for machine learning interatomic potentials. *Nat. Comput. Sci.* **3**, 998–1000 (2023).
54. Choudhary, K. et al. Recent advances and applications of deep learning methods in materials science. *npj Comput Mater.* **8**, 59 (2022).
55. Cheng, B. Cartesian atomic cluster expansion for machine learning interatomic potentials. *npj Comput. Mater.* **10**, 157 (2024).
56. Keith, J. A. et al. Combining Machine Learning and Computational Chemistry for Predictive Insights Into Chemical Systems. *Chem. Rev.* **121**, 9816–9872 (2021).
57. Elena, A. M. et al. Machine learned potential for high-throughput phonon calculations of metal—organic frameworks. *npj Comput Mater.* **11**, 125 (2025).
58. Schütt, K. et al. Schnet: A continuous-filter convolutional neural network for modeling quantum interactions. *Adv. Neural Inf. Process. Syst.* **30** (2017).
59. Chen, C., Ye, W., Zuo, Y., Zheng, C. & Ong, S. P. Graph Networks as a Universal Machine Learning Framework for Molecules and Crystals. *Chem. Mater.* **31**, 3564–3572 (2019).
60. Chen, C. & Ong, S. P. A universal graph deep learning interatomic potential for the periodic table. *Nat. Comput. Sci.* **2**, 718–728 (2022).
61. Ko, T. W. & Ong, S. P. Data-efficient construction of high-fidelity graph deep learning interatomic potentials. *npj Comput. Mater.* **11**, 65 (2025).
62. Deng, B. et al. CHGNet as a pretrained universal neural network potential for charge-informed atomistic modelling. *Nat. Mach. Intell.* **5**, 1031–1041 (2023).
63. Ko, T. W. et al. Materials Graph Library (MatGL), an open-source graph deep learning library for materials science and chemistry. *npj Comput Mater.* **11**, 253 (2025).
64. Li, X.-L. et al. Stabilizing Transition Metal Vacancy Induced Oxygen Redox by Co2+/Co3+ Redox and Sodium-Site Doping for Layered Cathode Materials. *Angew. Chem. Int. Ed.* **60**, 22026–22034 (2021).
65. Zhao, C. et al. Rational design of layered oxide materials for sodium-ion batteries. *Science* **370**, 708–711 (2020).
66. Wu, L.-T. et al. Prediction of Structural Stability of Layered Oxide Cathode Materials: Combination of Machine Learning and Ab Initio Thermodynamics. *Adv. Energy Mater.* e05470, https://doi.org/10.1002/aenm.202505470 (2025).
67. Köster, K., Binninger, T. & Kaghazchi, P. Optimization of Coulomb energies in gigantic configurational spaces of multi-element ionic crystals. *npj Comput. Mater.* **11**, 202 (2025).

68. Liu, Y. et al. Mitigation of Jahn–Teller distortion and Na+/vacancy ordering in a distorted manganese oxide cathode material by Li substitution. *Chem. Sci.* **12**, 1062–1067 (2021).
69. Li, Y. et al. Enhanced stability in a layered P2-Na0.67Fe0.5Mn0.5O2 cathode for sodium ion batteries via a synergistic Cu/Ti co-doping strategy. *Inorg. Chem. Front.* https://doi.org/10.1039/D5QI01070E (2025).
70. Jin, J. et al. Intrinsic distortion against Jahn-Teller distortion: a new paradigm for high-stability Na-ion layered Mn-rich oxide cathodes. *Angew. Chem. Int. Ed.* **64**, e202423728 (2025).
71. Tian, K. et al. Boosting electrochemical reaction and suppressing phase transition with a high-entropy O3-type layered oxide for sodium-ion batteries. *J. Mater. Chem. A* **10**, 14943–14953 (2022).
72. Xiong, X. et al. Atomic-level electric polarization in entropy-driven perovskites for boosting dielectric response. *Adv. Mater.* **37**, 2415351 (2025).
73. Pearson, R. G. Hard and soft acids and bases. *J. Am. Chem. Soc.* **85**, 3533–3539 (1963).
74. Pearson, R. G. Hard and soft acids and bases, HSAB, part 1: Fundamental principles. *J. Chem. Educ.* **45**, 581 (1968).
75. Pearson, R. G. Hard and soft acids and bases, HSAB, part II: Underlying theories. *J. Chem. Educ.* **45**, 643 (1968).
76. Murty, B. S., Yeh, J.-W., Ranganathan, S. & Bhattacharjee, P. P. *High-entropy alloys*. (Elsevier, 2019).
77. Zhang, R.-Z. & Reece, M. J. Review of high entropy ceramics: design, synthesis, structure and properties. *J. Mater. Chem. A* **7**, 22148–22162 (2019).
78. Takahashi, Y., Gotoh, Y. & Akimoto, J. Single-crystal growth, crystal and electronic structure of NaCoO2. *J. Solid State Chem.* **172**, 22–26 (2003).
79. Horton, M. K. et al. Accelerated data-driven materials science with the Materials Project. *Nature Materials*, https://doi.org/10.1038/s41563-025-02272-0 (2025).
80. Jain, A. et al. Commentary: The Materials Project: A materials genome approach to accelerating materials innovation. *APL Mater.* **1**, https://doi.org/10.1063/1.4812323 (2013).
81. Huang, Q. et al. Coupling between electronic and structural degrees of freedom in the triangular lattice conductor Na_xCoO_2. *Phys. Rev. B* **70**, 184110 (2004).
82. Blöchl, P. E. Projector augmented-wave method. *Phys. Rev. B* **50**, 17953–17979 (1994).
83. Kresse, G. & Joubert, D. From ultrasoft pseudopotentials to the projector augmented-wave method. *Phys. Rev. B* **59**, 1758–1775 (1999).
84. Kresse, G. & Hafner, J. Ab initio molecular dynamics for liquid metals. *Phys. Rev. B* **47**, 558–561 (1993).
85. Kresse, G. & Furthmüller, J. Efficiency of ab-initio total energy calculations for metals and semiconductors using a plane-wave basis set. *Comput. Mater. Sci.* **6**, 15–50 (1996).
86. Kresse, G. & Furthmüller, J. Efficient iterative schemes for ab initio total-energy calculations using a plane-wave basis set. *Phys. Rev. B* **54**, 11169–11186 (1996).
87. Perdew, J. P., Burke, K. & Ernzerhof, M. Generalized Gradient Approximation Made Simple. *Phys. Rev. Lett.* **77**, 3865–3868 (1996).
88. Grimme, S., Antony, J., Ehrlich, S. & Krieg, H. A consistent and accurate ab initio parametrization of density functional dispersion correction (DFT-D) for the 94 elements H-Pu. *J. Chem. Phys.* **132**, https://doi.org/10.1063/1.3382344 (2010).
89. Monkhorst, H. J. & Pack, J. D. Special points for Brillouin-zone integrations. *Phys. Rev. B* **13**, 5188–5192 (1976).
90. Pack, J. D. & Monkhorst, H. J. Special points for Brillouin-zone integrations"-a reply. *Phys. Rev. B* **16**, 1748–1749 (1977).
91. Jain, A. et al. Formation enthalpies by mixing GGA and GGA + *U* calculations. *Phys. Rev. B* **84**, 045115 (2011).
92. Jain, A. et al. A high-throughput infrastructure for density functional theory calculations. *Comput. Mater. Sci.* **50**, 2295–2310 (2011).
93. Nosé, S. A molecular dynamics method for simulations in the canonical ensemble. *Mol. Phys.* **52**, 255–268 (1984).
94. Hoover, W. G. Canonical dynamics: Equilibrium phase-space distributions. *Phys. Rev. A* **31**, 1695–1697 (1985).
95. Metropolis, N., Rosenbluth, A. W., Rosenbluth, M. N., Teller, A. H. & Teller, E. Equation of State Calculations by Fast Computing Machines. *J. Chem. Phys.* **21**, 1087–1092 (1953).

Acknowledgements

This work has been financially supported by the National Science and Technology Council, Taiwan (NSTC 113-2113-M-011-003-MY3, 114-2639-E-011-001-ASP, 115-2927-I-011-502, and 114-2923-E-011-001) and Sustainable Electrochemical Energy Development (SEED) Center supported by the Ministry of Education (MOE), Taiwan. The authors thank the Taiwan National Center of High-Performance Computing (NCHC) for computing resources. We also acknowledge support from the UMC Fellowship.

Author contributions

L.T.W., Z.L.L., and S.Y.Y. designed and performed the computations under the supervision of P.K. and J.C.J. All authors discussed the computational results. L.T.W. wrote the manuscript with support from Z.L.L. and S.Y.Y. P.K., and J.C.J. contributed to revising the manuscript. J.C.J. served as the lead principal investigator.

Competing interests

The authors declare no competing interests.

Additional information

Supplementary information The online version contains supplementary material available at https://doi.org/10.1038/s41524-025-01954-2.

Correspondence and requests for materials should be addressed to Jyh-Chiang Jiang.

Reprints and permissions information is available at http://www.nature.com/reprints

Publisher's note Springer Nature remains neutral with regard to jurisdictional claims in published maps and institutional affiliations.

Open Access This article is licensed under a Creative Commons Attribution-NonCommercial-NoDerivatives 4.0 International License, which permits any non-commercial use, sharing, distribution and reproduction in any medium or format, as long as you give appropriate credit to the original author(s) and the source, provide a link to the Creative Commons licence, and indicate if you modified the licensed material. You do not have permission under this licence to share adapted material derived from this article or parts of it. The images or other third party material in this article are included in the article's Creative Commons licence, unless indicated otherwise in a credit line to the material. If material is not included in the article's Creative Commons licence and your intended use is not permitted by statutory regulation or exceeds the permitted use, you will need to obtain permission directly from the copyright holder. To view a copy of this licence, visit http://creativecommons.org/licenses/by-nc-nd/4.0/.

© The Author(s) 2026